Available online at www.sciencedirect.com

SCIENCE DIRECT®

Earth and Planetary Science Letters 234 (2005) 119–134

EPSL

www.elsevier.com/locate/epsl

The seismological signature of temperature and grain size variations in the upper mantle

Ulrich H. Faul*, Ian Jackson

Research School of Earth Sciences, The Australian National University, Canberra, ACT 0200, Australia

Received 20 July 2004; received in revised form 11 November 2004; accepted 10 February 2005
Available online 22 April 2005
Editor: R.D. van der Hilst

Abstract

The shear modulus and attenuation of pure and therefore genuinely melt-free polycrystalline aggregates of Fo_{90} olivine have recently been measured over a wide range of mean grain size at upper mantle temperatures and seismic frequencies [1,2] [B.H. Tan, I. Jackson, J.D. Fitz Gerald, High-temperature viscoelasticity of fine-grained polycrystalline olivine, Phys. Chem. Miner. 28 (2001) 641–664; I. Jackson, J.D. Fitz Gerald, U.H. Faul, B.H. Tan, Grain-size sensitive seismic wave attenuation in polycrystalline olivine, J. Geophys. Res. 107 (B12 2360) (2002) doi:10.1029/2001JB001225]. Here for the first time we fit the experimental shear modulus and attenuation data to a common model that provides an internally consistent description of the observed variations with frequency, temperature and grain size. This model is used to perform indicative calculations of shear wave speed (V_s) and attenuation (Q) along geotherms representative of both oceanic and continental settings, intended to highlight the sensitivity of V_s and Q to variations of temperature and grain size. Comparison of the results of these calculations with seismological models suggests the following: (1) The low velocity zone (LVZ), commonly observed below ocean basins, and its tendency to become less pronounced and deeper with increasing lithospheric age, can be explained by solid state mechanisms without the presence of melt or fluids. (2) The relatively large velocity variations in the upper mantle seen in global tomographic models can be explained by reasonable temperature differences within continents and between continents and oceans. (3) The velocity increase below ~200 km seen in most seismological models may indicate an increase in grain size from order of mm in the shallow upper mantle to ~cm above the transition zone.

Keywords: shear velocity; attenuation; low velocity zone; lithosphere; olivine

1. Introduction

Inferring the physical state of the upper mantle from regional and global seismological models has been the aim of number of recent papers (e.g. [3–7]). While it is widely accepted that most of the variability in wave speeds seen in these models is due to variations in temperature, conversion of velocities to temperatures has been hampered by lack of direct measurements of the shear modulus of olivine at high temperatures and seismic frequencies. The contribu-

* Corresponding author.
E-mail address: uli.faul@anu.edu.au (U.H. Faul).

0012-821X/$ - see front matter © 2005 Elsevier B.V. All rights reserved.
doi:10.1016/j.epsl.2005.02.008

tion of anelasticity to the temperature sensitivity of shear wave velocities has previously only been estimated indirectly through the temperature sensitivity of attenuation (Q) [8,9]. Here we use for the first time simultaneous laboratory measurements of shear modulus and Q at seismic frequencies and mantle temperatures [1,2] to constrain temperatures in both oceanic and continental upper mantle.

Among the key questions regarding the structure of the upper mantle are the thickness of continental roots [10] and the origin of the zone of low seismic shear wave velocity in the Earth's upper mantle. This low velocity zone (LVZ) is commonly equated with a zone of low viscosity that facilitates the movement of tectonic plates (e.g. [11]). However, the physical mechanisms giving rise to the low-velocity, high-attenuation zone have been the subject of debate since it was first discovered more than 50 years ago [12]. Partial melting is usually invoked to explain the low velocity zone [13], but the presence of water has also been suggested [14]. Goetze [15] suggested a solid-state mechanism, but no directly relevant laboratory data were then available to support this hypothesis.

In the following we describe the procedure for fitting the experimental data and then use the fits to calculate temperatures for the oceanic upper mantle for conductively cooling lithosphere overlying adiabatic mantle. For continents, the calculated geotherms include heat production in upper and lower crust and mantle lithosphere. The geotherms are constrained by the observed surface temperature and heat flow. We use the new laboratory data to show that many first-order features of the seismologically observed structure of the olivine-dominated upper mantle for both oceans and continents can be explained by the transition in dry crystalline material from elastic to viscoelastic behaviour, along with the competing effects of temperature and pressure on the shear modulus of olivine.

2. Description of the experimental shear modulus and attenuation data by a creep function

During the past few years the application of seismic-frequency laboratory methods has begun to revolutionize our understanding of seismic wave speeds and attenuation in olivine-dominated upper-mantle materials [16,17]. The observed modulus reduction and enhanced attenuation at high temperatures are most plausibly explained by grain boundary sliding [2,16,18–22].

Microcreep tests on olivine polycrystals show that their mechanical response to the application of a step-function stress is characterized by three distinct regimes [2]. The instantaneous, elastic response is followed by a transient, anelastic strain that is recoverable, and lastly by permanent (irrecoverable) viscous deformation. This behavior is qualitatively that of a Burgers model solid, consisting of a suitable combination of springs and dashpots (e.g. [23], Ch. 3; [24], Ch. 4.5, 4.6 and 6.5).

The time-dependent response (strain) of the Burgers model system to application at time $t=0$ of unit step-function stress defines the creep function:

$$J(t) = J_{\mathrm{U}}\left\{1 + \Delta\left(1 - e^{-\frac{t}{\tau}}\right) + \frac{t}{\tau_{\mathrm{M}}}\right\} \tag{1}$$

where J_{U} is the unrelaxed compliance, given by the reciprocal of the unrelaxed (elastic) shear modulus G_{U}. The anelastic relaxation strength Δ is given by $\Delta=(G_{\mathrm{U}}-G_{\mathrm{R}})/G_{\mathrm{R}}$, with G_{R} the relaxed modulus (anelastic relaxation only). The Maxwell relaxation time associated with the steady state (Newtonian) viscous element of viscosity η is given by:

$$\tau_{\mathrm{M}} = \eta J_{\mathrm{U}}. \tag{2}$$

The Debye-type anelastic relaxation of this simple Burgers model solid involves a unique relaxation time τ. However, seismological observations of a broad absorption band within which Q^{-1} varies weakly with frequency indicate that a distribution of relaxation times is required. Anderson and Minster [8] introduced a normalized distribution of relaxation times as

$$D(\tau) = \frac{\alpha_Q \tau^{\alpha_Q - 1}}{\tau_{\mathrm{H}}^{\alpha_Q} - \tau_{\mathrm{L}}^{\alpha_Q}},\ \tau_{\mathrm{L}} < \tau < \tau_{\mathrm{H}} \tag{3}$$

between the lower and upper cutoff times τ_{L} and τ_{H} and zero elsewhere. They suggested that the upper and lower cutoff times depend on physical and geometrical variables as well as thermodynamic conditions. The seismologically inferred value for

the parameter α_Q, which characterizes the weak frequency dependence, is very similar to the value much more tightly constrained by experiments (e.g. [2,16]).

The temperature and grain size dependence of the Maxwell relaxation time (Eq. (2)) is derived from the temperature and grainsize dependence of the viscosity $\eta \sim d^m \exp(E/RT)$ (e.g. [18,24]) and expressed in the following form:

$$\tau = A d^m e^{\left(\frac{E}{RT}\right)} \tag{4}$$

where A is a constant, E is the activation energy, R is the gas constant, T is absolute temperature and d is the grain size with exponent m.

The experimental observations confirm the suggestion of Anderson and Minster [8] that the cutoff times for the distribution of anelastic relaxation times are similarly temperature and grain size dependent. For example, the deviation from linearity of attenuation in log–log space at the longest periods and highest temperatures for the most fine-grained sample (Fig. 1c) indicates the transition from anelastic to viscous behavior. Such variations with grain size and temperature are conveniently expressed by a modified version of Eq. (4):

$$\tau_i = \tau_{iR} \left(\frac{d}{d_R} \right)^m e^{\left\{ \left(\frac{E}{R}\right) \left(\frac{1}{T} - \frac{1}{T_R}\right) \right\}}, \tag{5}$$

where the τ_i are the upper and lower cutoff times (τ_L and τ_H) and the Maxwell time (τ_M). The parameters τ_{iR} are the values of the τ_i at the reference temperature T_R and the reference grain size d_R [22]. Different grain-size exponents m_A for τ_L and τ_H,

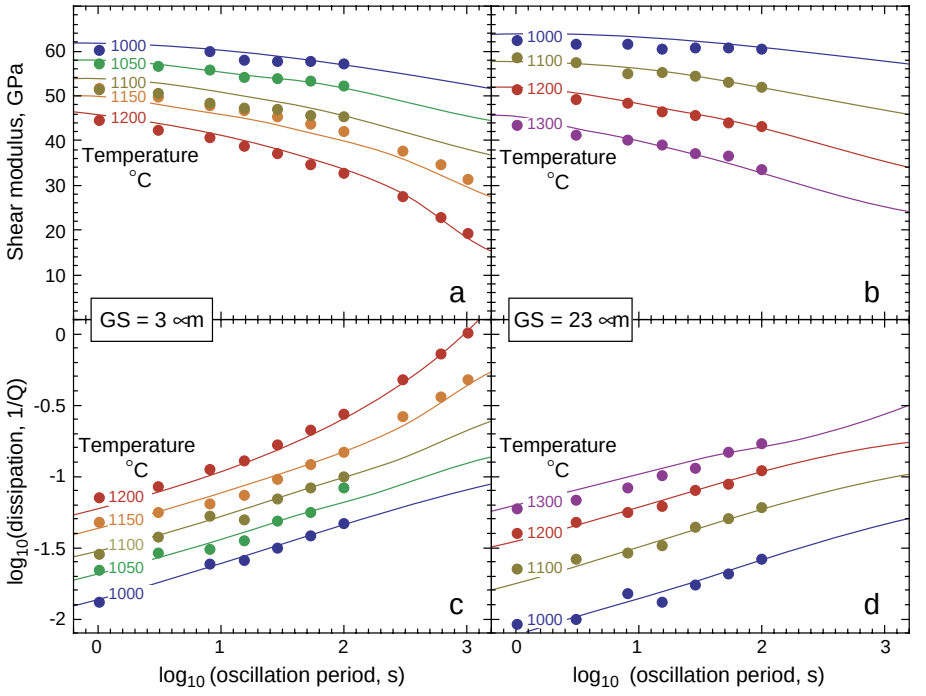

Fig. 1. Shear modulus and strain energy dissipation as functions of temperature and period for two samples differing by nearly one order of magnitude in grain size. When plotted in log–log space the dissipation clearly shows the mild period dependence with near constant exponent α_Q characteristic of anelastic behaviour. Only at the highest temperatures and longest periods for the fine-grained sample is the transition to viscous behaviour evident. The grain size dependence is clearly evident when comparing shear modulus or attenuation of the two samples at a fixed temperature. The dots represent the experimental data, the lines the extended Burgers model fit given by Eqs. (11)–(14).

Table 1
Parameters of the Burgers model

Parameter	Unit	Value	Uncertainty
d_R	m	1e−5	
T_R	K	1223	
J_U	GPa^{-1}	0.0149	0.0001
$\partial \ln J_U/\partial T$	K^{-1}	9.1e−4	7e−5
Δ		1.4	[a]
α_Q		0.270	0.008
τ_L		3.981e−3	[a]
τ_H		5.26e6	1.55e6
τ_M		4.31e6	2.38e6
m_A		1.09	0.05
m_J		0.16	0.02
m_V		2.1	0.4
E	J mol^{-1}	5.05e5	0.5e5
Additional parameters			
V^*	m^3 mol^{-1}	1.2e−5	
$(\partial G/\partial T)_{anh}$	GPa K^{-1}	−0.0136	[25]
$(\partial G/\partial P)_{anh}$		1.8	[27]

Parameters derived from non-linear least-squares fit of data from four specimens from Tan et al. [1] (AT6261, full 1000–1300 °C dataset; AT 6328, 1100 and 1200 °C data) and Jackson et al. [2] (AT6381, 1000–1200 °C dataset without 305–1022 s data at 1050 °C and 3 s data at 1000 °C; AT6365 full 1000–1200 °C dataset) to Eqs. (13) and (14).

[a] τ_L is not very well constrained experimentally (Sections 2 and 5), and Δ covaries with τ_L/τ_H.

and m_V for τ_M are allowed (Table 1), reflecting the different diffusion distances involved in anelastic and viscous relaxation.

The experimental data presented in Fig. 1 from two representative melt-free specimens shows their high temperature, viscoelastic behavior characterized by systematic variation of both shear modulus and attenuation with period, temperature and grain size. We observe the transition from elastic to viscoelastic behavior near 900 °C in the form of an appreciable enhancement of the temperature sensitivity of G and Q ([1], their Fig. 10). To capture this behavior, and to incorporate pressure dependence, Eq. (1) has to be suitably modified to:

$$J(t,d,T,P) = J_U(P)\left(1 + \delta\ln J_U + \Delta\int_{\tau_L}^{\tau_H} D(\tau) \times \left(1 - e^{-\frac{t}{\tau}}\right)d\tau + \frac{t}{\tau_M}\right) \quad (6)$$

where $J_U(P)$ is the unrelaxed compliance with its usual anharmonic (elastic) pressure dependence.

The term $\delta\ln J_U$ is a fractional adjustment to J_U, which in the elastic regime (below about 900 °C) is simply the anharmonic temperature dependence of J_U (e.g. [25]). Within the viscoelastic regime (above about 900 °C) the unrelaxed shear modulus ($G_U = J_U^{-1}$) fitted to data for periods of 1–1020s is found to be more strongly temperature dependent than can be reconciled with the simple anharmonic temperature sensitivity of G_U. This suggests that the distribution of anelastic relaxation times must extend well below 1 s (i.e. $\tau_L < 1$ s). This lower end of the distribution is not well constrained by our current experiments. Since this additional relaxation is anelastic in nature it should be grain-size sensitive, as observed. To account for this additional relaxation we define for the viscoelastic regime:

$$\delta\ln J_U = \left(\frac{\partial \ln J_U}{\partial T}\right)_R \left(\frac{d}{d_R}\right)^{-m_J}(T - T_R). \quad (7)$$

As part of our fit to the data, the unrelaxed modulus at the reference temperature of 950 °C is found to be 67.1 GPa. Using the anharmonic temperature derivative of −0.0136 GPa/K [25], this corresponds to a shear modulus at room temperature of 80 GPa, within the upper end of the range of experimentally determined values [26].

For the application of a periodic shear stress in our torsional forced oscillation experiments the stress can be expressed as:

$$\sigma(t) = \sigma_0 e^{i\omega t} \quad (8)$$

where σ_0 is the stress amplitude and ω the circular frequency. The resulting shear strain lags behind by an angle ϕ:

$$\epsilon(t) = \epsilon_0 e^{i(\omega t - \varphi(\omega))}. \quad (9)$$

The complex compliance $J^*(\omega)$

$$J^*(\omega) = \frac{\epsilon(t)}{\sigma(t)} = ||J(\omega)||e^{-i\varphi(\omega)} = J_1(\omega) - iJ_2(\omega) \quad (10)$$

is essentially the Laplace (or Fourier) transform of $J(t)$ [23]. The frequency dependent shear modulus G and

strain energy dissipation Q^{-1} are calculated as follows:

$$G(\omega) = (J_1^2(\omega) + J_2^2(\omega))^{-\frac{1}{2}} \tag{11}$$

and

$$Q^{-1} = \frac{J_2(\omega)}{J_1(\omega)} \tag{12}$$

with

$$J_1(\omega, d, T, P) = J_U(P)\left(1 + \delta \ln J_U + \frac{\alpha_Q \Delta}{\tau_H^{\alpha_Q} - \tau_L^{\alpha_Q}} \times \int_{\tau_L}^{\tau_H} \frac{\tau^{\alpha_Q - 1}}{1 + \omega^2 \tau^2} \mathrm{d}\tau\right) \tag{13}$$

and

$$J_2(\omega, d, T, P) = J_U(P)\left(\frac{\omega \alpha_Q \Delta}{\tau_H^{\alpha_Q} - \tau_L^{\alpha_Q}} \int_{\tau_L}^{\tau_H} \frac{\tau^{\alpha_Q}}{1 + \omega^2 \tau^2} \mathrm{d}\tau + \frac{1}{\omega \tau_M}\right) \tag{14}$$

This rheology with suitably optimised values of the model parameters given in Table 1 provides an entirely adequate description of the variation with period (1–1020 s), temperature (1000–1300 °C) and grain size (3–165 μm) of both the shear modulus and dissipation measured for genuinely melt-free olivine polycrystals [1,2] (Fig. 1).

The large dataset, comprising a total of 206 individual measurements of shear modulus and dissipation on four specimens, allows the refinement of the 9 model parameters (Table 1) needed to fully specify the creep function. The advantage of this approach is that the transition from elastic through anelastic to viscous behaviour is captured in a way that provides for an internally consistent treatment of the modulus and dissipation. Thus this model, unlike the simpler Q^{-1}-period power-law alternative (e. g., [2]), accommodates the systematic trend towards more strongly frequency-dependent Q^{-1} with increasing period for the fine-grained specimen of Fig. 1.

On application of the Burgers model to upper mantle conditions our experimental data require only moderate extrapolation in grain size and temperature (Fig. 2). In the calculations below, we account for the effect of pressure P on both shear modulus and attenuation by using the anharmonic derivative ($\mathrm{d}G/\mathrm{d}P = 1.8$ [27]) and scaling the relaxation times (Eq. (5)) by a factor $\exp(PV^*/RT)$ with a suitable activation volume V^* (see Section 4.2). The period in the calculations is roughly scaled to depth as appropriate for surface waves [28].

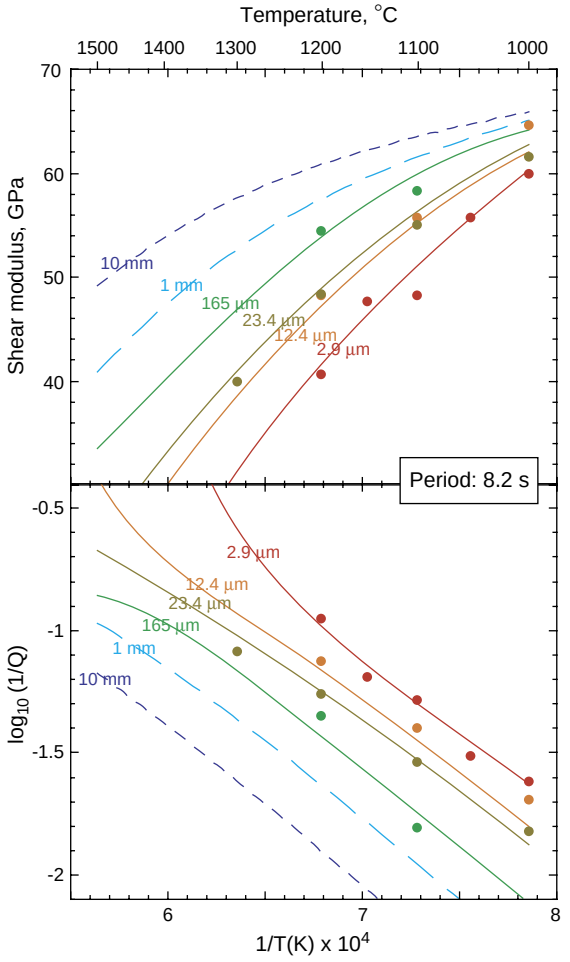

Fig. 2. Shear modulus and dissipation as functions of inverse temperature, contoured for grain size at a representative fixed period of 8.2 s. Dots represent experimental data, solid lines the extended Burgers model fit at the corresponding grain size. Dashed lines indicate extrapolation in grain size; only a modest extrapolation in temperature is necessary for upper mantle conditions. At a fixed temperature the shear modulus increases and attenuation decreases with increasing grain size.

3. Temperature calculation

3.1. Adiabat and geotherm beneath ocean basins

Adiabatic temperatures are calculated from

$$T_{\mathrm{ad}} \approx T_0\left(1+\frac{\alpha_{\mathrm{T}} g z}{c_{\mathrm{p}}}\right), \tag{15}$$

where T_0 is the potential temperature, z is depth and g is acceleration due to gravity (e.g. [29]). The coefficient of thermal expansion α_{T} and specific heat at constant pressure c_{p} are assumed to be independent of pressure and temperature. With potential temperatures between 1300 and 1400 °C, adiabatic temperatures at 400 km depth do not exceed 1550 °C. Over this temperature range c_{p} varies by less than 4% around an approximate value of 1350 J kg^{-1} K^{-1} [30]. The variation in the coefficient of thermal expansion in this temperature range is larger, and it is also significantly pressure dependent. On an adiabat with a potential temperature of 1300 °C from 100 to 400 km depth, α_{T} decreases from ~3.5×10^{-5} K^{-1} to ~2.3×10^{-5} K^{-1} [31]. We used $\alpha_{\mathrm{T}}=2.9\times10^{-5}$ K^{-1} in our calculations, but the decrease in α_{T} with depth means that adiabatic temperatures are overestimated below 200 km and hence velocities somewhat underestimated.

Density and pressure are calculated with constant adiabatic compressibility β_{a} from [29]:

$$\rho=\frac{\rho_0}{1-\rho_0 g\beta_{\mathrm{a}} z} \text{ and } P=\frac{-\ln(1-\rho_0 g\beta_{\mathrm{a}} z)}{\beta_{\mathrm{a}}} \tag{16}$$

It is well established that the structure and properties of oceanic lithosphere up to ages of 80–100 My are consistent with a conductively cooling half-space model. Age-dependent geotherms can be calculated from [29]:

$$T=T_{\mathrm{S}}+(T_{\mathrm{ad}}-T_{\mathrm{S}})\mathrm{erf}\left(\frac{z}{2\sqrt{(\kappa t)}}\right) \tag{17}$$

where T_{S} is the temperature at the ocean floor, t is the age of the ocean floor and κ is the thermal diffusivity. Again κ is assumed constant, but experimentally determined values decrease by a factor of two in the temperature range from 300 to 1000 °C, and are constant only at higher temperatures [32]. If the observed decrease is taken into account, temperature gradients are less steep below 800 °C and steeper from 800–1200 °C. Above 1200 °C the temperatures are the same as for constant κ [33].

3.2. Continental geotherms

Temperatures in the continental lithosphere are calculated for a model that includes different values for heat production and conduction in upper and lower crust as well as the lithospheric part of the mantle. Following Chapman [34] temperature and heat flow q are calculated from:

$$T_{\mathrm{b}}=T_{\mathrm{t}}+\frac{q_{\mathrm{t}}}{k}\Delta z-\frac{\rho H}{2k}\Delta z^2 \text{ and } q_{\mathrm{b}}=q_{\mathrm{t}}-\rho H\Delta z \tag{18}$$

where the subscripts t and b indicate top and bottom of a layer with thickness Δz, k is the thermal conductivity and ρH the volumetric heat production. Fig. 3 shows the boundary conditions used in the calculations.

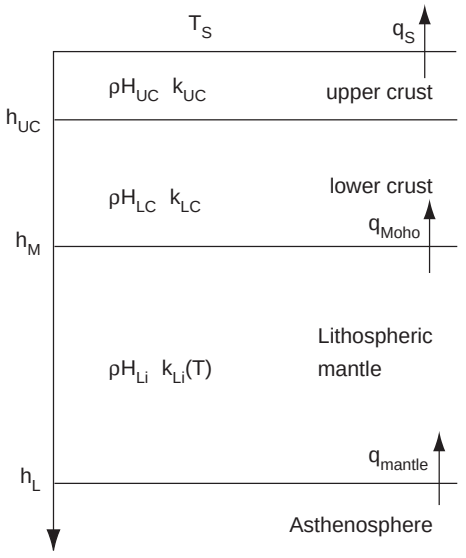

Fig. 3. Sketch of the three-layer model used in the calculation of continental geotherms. Surface temperature, surface heat flow and Moho depth are given by McLaren et al. [48] and Clitheroe et al. [49], respectively. Thermal conductivity in upper and lower crust is fixed ($k_{\mathrm{UC}}=k_{\mathrm{LC}}=2.5$ W m^{-2}). This is an oversimplification but results only in a small trade-off with heat production for the same geotherm. k_{Li} is calculated as a function of temperature from Eq. (19).

The thermal conductivity in the crust is fixed, thermal conductivity in the mantle part of the lithosphere is calculated from [35]

$$k(T) = \frac{1}{0.174 + 0.000265T} + 3.68 \times 10^{-10} T^3. \quad (19)$$

Changes in the values of thermal conductivity are compensated by slight changes in heat production to result in essentially the same geotherm. The intersection of the geotherms with the adiabat is smoothed to avoid artificial kinks in the velocity-depth profiles.

4. Results

4.1. Oceans

Fig. 4 shows adiabats and resulting shear velocity and Q calculated for 100 My old oceanic lithosphere. Also shown in Fig. 4b is the model PA5 of Gaherty et al. [36] for the Tonga-Hawaii corridor for which the age of the oceanic crust is close to 100 My. Below the crust (which is not modelled) there is a moderate decrease in the calculated velocity to a depth of ~80 km corresponding to 900 °C. At greater depths, the stronger temperature sensitivity due to viscoelastic

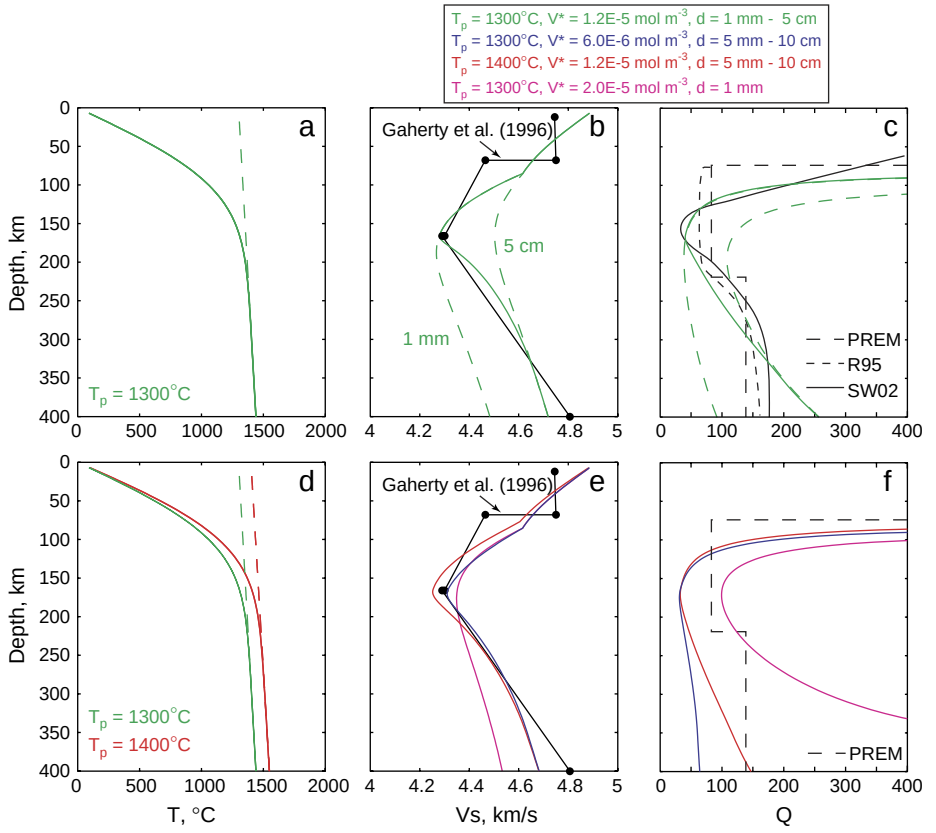

Fig. 4. Calculated and observed velocity structure of 100 My old oceanic lithosphere. (a–c) Shear velocity and Q for a geotherm joining a 1300 °C adiabat (dashed line in (a)). Shear velocity and Q are calculated with the extended Burgers model given by Eqs. (11)–(14). Dashed lines in (b) and (c) are calculated for fixed grain sizes of 1 mm and 5 cm, respectively. The solid lines illustrate the effect of a gradual increase in grain size from 1 mm to 5 cm with increasing depth below 165 km. The black line in (b) is the isotropic model PA5 (V_{SV} and V_{SH} averaged) of Gaherty et al. [36], the gray lines in (c) are different Q models [39–41]. (d–f) Effects of varying temperature and activation volume. A higher adiabatic temperature (labelled III) can be compensated by increasing the grain size, resulting in a shear velocity structure (e) that is essentially indistinguishable to that shown in (b), but somewhat lower Q (f). A lower activation volume (II) can be compensated for by increasing the grain size (e) but Q is substantially too low relative to the seismological models (f). A higher activation volume with a constant grain size of 1 mm (IV) results in a shear velocity that is too high above 150 km depth but too low below (e), and too high Q (f).

behaviour combines with the still large temperature gradients in the conductively cooling part of the lithosphere. The velocity minimum occurs at ~170 km depth, where the conductive part of the geotherm grades into the adiabat with its much smaller temperature gradient.

The increase in velocity at greater depth is due to the pressure effect on the shear modulus, which overwhelms the modest temperature induced decrease. Anharmonic, viscoelastic and pressure effects on the shear modulus of melt-free olivine thus combine to produce a pronounced low velocity zone. With variable thermal diffusivity [33] (see Section 3.1), the shallow lithospheric velocity gradients would be somewhat reduced, and the onset of the low velocity zone somewhat more pronounced.

Velocities calculated with a (uniform) grain size of 1 mm are significantly lower deeper than ~200 km than those of seismological models [36–38], while those calculated with a grain size of 5 cm do not match the velocity minimum shown by these models (Fig. 4b). One way to match the increase in shear velocity below the LVZ is to progressively increase the grain size by about one order of magnitude from ~mm to ~cm. The increase in grain size is modeled to begin below 165 km depth where Gaherty et al. [36] find that significant anisotropy is no longer resolvable. The maximum grain size is reached at 350 km depth.

Fig. 4c shows a comparison of Q calculated with the same parameters as V_s in Fig. 4b with seismological Q models. The important point here is that both V_s and Q are calculated self consistently, and simultaneously match seismological V_s and Q models.

Fig. 4d–f illustrate the trade-offs between temperature, grain size and activation volume. A higher potential temperature (1400 °C) can be partially compensated by a correspondingly larger grain size. The fit to the V_s model is still satisfactory while the calculated Q is somewhat low relative to the seismological models. Similarly, a lower activation volume can be compensated by a larger grain size for V_s, but since global Q models show a recovery from the minimum in the LVZ [39–41], Q does not fit the models as well. Increasing V^* from the preferred value of 1.2×10^{-5} m^3 mol^{-1} to 2×10^{-5} m^3 mol^{-1} while keeping the grain size fixed at 1 mm does not fit either V_s or Q models.

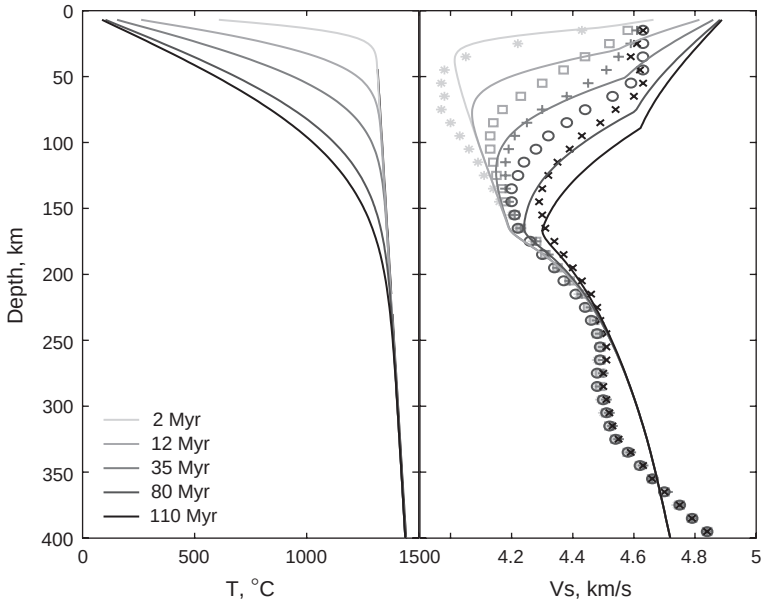

Fig. 5. Age dependence of depth and magnitude of the velocity reduction of the LVZ. (a) Geotherms as a function of age for conductively cooling oceanic lithosphere, and (b) the corresponding shear velocities. The symbols are from a model by Nishimura and Forsyth [37], the solid lines are the velocities calculated for the geotherms in (a). The ages shown in (a) correspond to the middle of the age range for the seismological model.

The need to match both V_s and Q models places therefore relatively tight constraints on V^*, while there is some trade off possible between temperature and grainsize. The parameters for V^* and T_p shown in Fig. 4a–c are used in all the following calculations. Our preferred value of V^* is well within the range of the available experimental estimates (e.g. [42,43]); it is also possible that V^* is pressure dependent (e.g. [44]).

The increase in the LVZ shear velocity minimum and its deepening with age have been observed in a number of seismological studies [37,45]. Fig. 5 shows a comparison of calculated velocities with the seismological model of Nishimura and Forsyth [37] for the same ages. The main features of an increasing velocity minimum in the LVZ and its deepening with age are clearly reproduced. For the youngest lithosphere the seismological indications of a deeper and more pronounced LVZ than calculated are suggestive of an additional velocity reduction due to the presence of melt, for example beneath the East Pacific Rise. For ages greater than 80–100 My it has previously been noted that the high-velocity lid approaches a constant thickness (e.g. [28] and references therein).

4.2. Continents

4.2.1. Background

Seismic velocities calculated for continental geotherms are compared with three different velocity-depth profiles extracted from a recent surface wave model of the Australasian region by Fishwick et al. [38]. This model is an extension of the Debayle and Kennett model [46] with additional data for Western Australia including both fundamental and higher

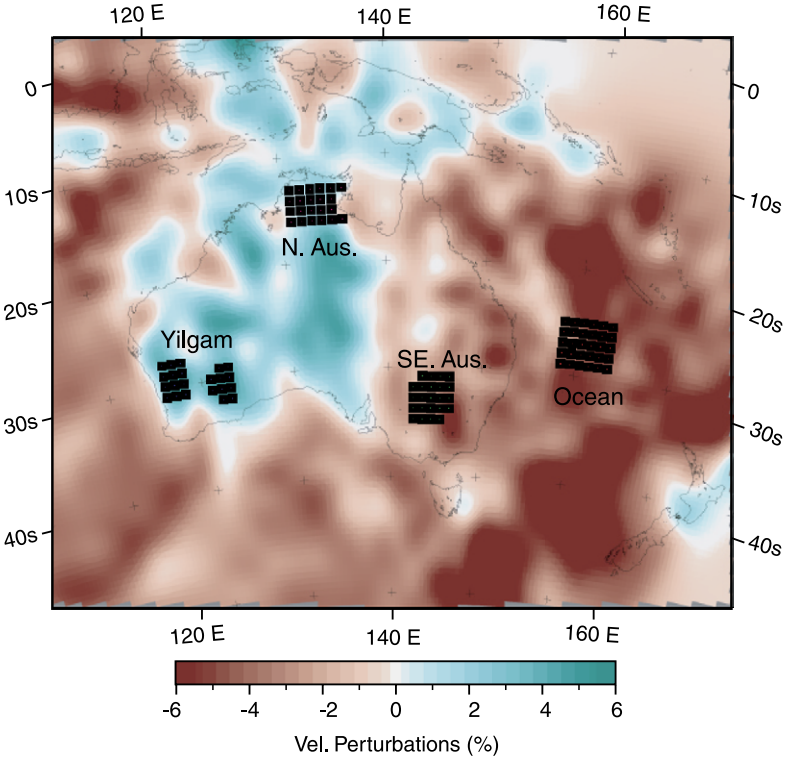

Fig. 6. Tomographic image of the shear velocities at 200 km depth of Australia and surrounding oceans from Fishwick et al. [38]. The squares indicate the locations of the three continental and one oceanic area for which the averaged model velocity structures are compared with calculated ones. The locations were chosen to sample relatively uniform velocity structures of the three major geologic regions in Australia: the Archean Yilgarn craton, Proterozic terrains that have high heat flow relative to global averages of terrains of the same age, and Paleozoic southeastern Australia. Inclusion of an averaged velocity depth profile from the Tasman Sea/Lord Howe Rise covers the shear velocity variations of nearly ±8% generally seen in global and regional models.

Table 2
Modelling results for Australia

	q_S (mW m^{-2})	h_M (km)	h_{UC} (km)	ρH_{UC} (μW m^{-3})	ρH_{LC} (μW m^{-3})	T_M (°C)	q_M (mW m^{-2})	q_L (mW m^{-2})
Yilgarn	51	37	6.6	2.2	0.8	430	12.2	1.3
N. Australia	83	42	9.8	4.0	1.0	630	11.6	0.9
SE Australia	79	39	11.2	3.0	1.0	650	17.6	6.8

modes. The seismic velocity-depth profiles represent three geologically different parts of the continent: the Archean Yilgarn craton in the Southwest, Proterozoic parts of the Northern Territory and Phanerozoic South-Eastern Australia (Fig. 6) and thus three different Australian heat flow provinces [47]. The average surface heat flow for each province is given by McLaren et al. [48] (see Table 2). The total crustal thickness at each location (h_M) is derived from Clitheroe et al. [49].

The seismic velocity-depth profiles are averages of more than 20 grid points through the model of Fishwick et al. [38]. In order to find the geotherm that produces the closest match in shear velocities to the seismological model a grid search is performed over upper and lower crustal heat production (ρH_{UC} and ρH_{LC}) as well as upper crustal thickness h_{UC}. The ranges used in the grid search (ρH_{UC}=1–5 μW m^{-3}, ρH_{LC}=0.2–1 μW m^{-3}, h_{UC}=5–12 km) are based on work by McLaren et al. [48]. The value for lithospheric mantle heat production (ρH_{Li}=0.03 μW m^{-3}) is taken from Rudnick et al. [50]. The mismatch between calculated velocities and the seismological model is estimated by calculating an rms misfit.

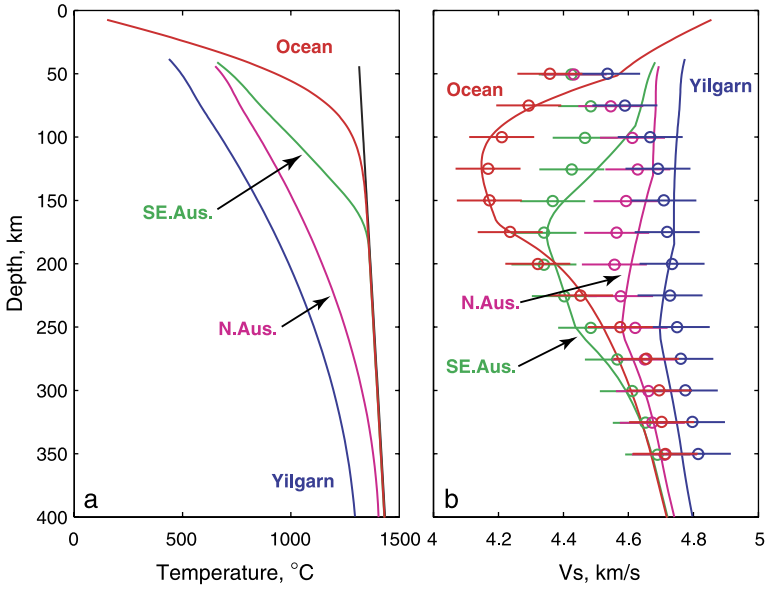

Fig. 7. (a) Geotherms and (b) corresponding velocities (solid lines) calculated for the locations shown in Fig. 6. The symbols are averages calculated through the model of Fishwick et al. [38], the horizontal bars indicate standard deviations. Thermal parameters and grain sizes used in the calculations are given in Tables 2 and 3. Dashed line in (a) indicates the 1300 °C adiabat. The oceanic geotherm was calculated as those in Figs. 4 and 5 for 35 My old lithosphere, the approximate age for this region of the Tasman Sea [63]. The parameters used in the calculations were kept as simple and uniform as practical, no attempt was made to match second order variations in the seismic velocity model (e.g. increase the grain size in the oceanic profile at 300 km depth and below to increase the calculated velocities). To first order all profiles other than for the Yilgarn craton can be matched with a common adiabat and a lower grain size of 5 cm. The largest velocity differences between relatively young oceanic lithosphere and archean craton are found between 100 and 200 km depth, corresponding to temperature differences of around 500–600 °C.

4.2.2. Results

Geotherms that satisfy the heat flow constraints and best fit the surface wave model for Australia are shown in Fig. 7. Table 2 shows the corresponding thermal parameters and Table 3 lithospheric thickness and grain sizes. It is not possible to construct geotherms that result in strongly positive velocity-depth gradients in the upper 100 km, as this is the depth region with the highest sub-crustal temperature gradients, which inherently lead to negative velocity gradients. Accordingly, the 50 km and 75 km points of the seismological model are not considered in the misfit calculations.

The seismological model shows high velocities at all depths for the Yilgarn craton; these can only be matched for significantly sub-adiabatic temperatures extending to the transition zone. Temperatures below Northern Australia are also sub-adiabatic to at least 300 km; the geotherm approaches the adiabat asymptotically below this depth, so that the lithospheric thickness is not well defined. The lithosphere beneath South-Eastern Australia is relatively thin, consistent with its lesser age and widespread Cenozoic magmatism. Simons et al. [51] similarly found an age dependence of the seismically detected lithospheric thickness; our somewhat different thickness estimates for Western Australia may be related to the increased coverage of this area by the data set of Fishwick et al. [38].

The deeper transition to larger grain size relative to the oceanic models (Table 3) reflects the greater depth to which anisotropy is observed beneath Australia [46,52]. Beneath the Tasman Sea the transition depth for the increase in grain size is the same as for the Pacific models (Table 3).

Table 3
Modelling parameters and results

	Lithospheric thickness (km)	T at 400 km depth (°C)	Grain size transition depth (°C)	Range in grain size (cm)
Yilgarn	400	1310	250–350	0.5–5
N. Australia	370	adiabatic	250–350	0.5–5
SE Australia	175	adiabatic[a]	250–350	0.5–5
Tasman Sea	135	adiabatic	165–350	0.1–5
Tonga-Hawaii	230	adiabatic	165–350	0.1–5
Pacific	age dependent	adiabatic	165–350	0.1–5

[a] The adiabatic temperature at 400 km depth for an adibat with a potential temperature of 1300 °C is ~1440 °C.

Calculated geotherms for the Yilgarn craton and Northern Australia are comparable to geotherms determined by Jaupart and Mareschal [35] for Eastern Canadian provinces of the same age. One of their main conclusions was that the heat flow across the Moho is relatively low, which is also the case in our models (Table 2). The anomalously high heat flow observed in Proterozoic regions of Australia is therefore due to relatively high upper crustal heat production, since the seismological model indicates high velocities and hence relatively low temperatures in the 100–300 km depth range. Moreover, when heat production in the mantle portion of the lithosphere is included, the heat-flow from the convecting mantle into the lithosphere is very small. South Eastern Australia is somewhat different in this regard, possibly related to the more recent magmatism.

5. Discussion

5.1. General

Our main aim is to explore how much of the range in velocities observed in continental and oceanic shear wave models can be explained by temperature variations. Our modeling, based on new seismic frequency laboratory data, sought to produce reasonable fits to the seismological models while remaining as simple as possible. The seismological models in this study were chosen because they covered specific regional settings. The main features of those models (LVZ and its age dependence for the Pacific Ocean, substantial high velocity lid below continents, relative velocity variations of up to $\pm 8\%$) are typical of the much wider suite of published models.

Features which we could not match with our modeling are the constant velocity lid for the Pacific ([36,37]) and the constant or increasing velocities below the crust of the Australian model [38]. Our thermal models like those of Karato and Jung [14] predict decreasing velocities in this depth interval with the highest temperature gradients (see also Section 5.4). With thermal constraints in inversions, Shapiro and Ritzwoller [53] found that for oceanic lithosphere negative gradients in the lid (rather than constant velocity) are compatible with their surface wave data.

Similarly for continents they reject models with positive gradients in the shallow lithosphere in favor of slightly negative gradients, consistent with our modeling.

5.2. Experimental

As highlighted in Section 2 we do not extrapolate very far in temperature or grain size from our experimental conditions in the application of our data to the mantle. The similarity of the exponent of the powerlaw behavior of attenuation in the anelastic regime from laboratory measurements and seismological observations has recently been confirmed by Shito et al. [54], who also emphasized that a value of α_Q between 0.2 and 0.4 is inconsistent with the presence of melt. Moreover, the activation volume, needed to constrain the pressure dependence of the relaxation times, is apparently relatively well constrained by seismological observation of V_s and Q (Fig. 4). Although we have established a robust experimentally based model for the viscoelastic behavior of polycrystalline olivine, some aspects of the data and modeling require further investigation.

The upper cutoff time and the Maxwell time have different sensitivities to grain size (i.e. $m_A < m_V$, Table 1). At small grain sizes, τ_H and τ_M are close, but they separate at larger grain sizes. Because the steady state behaviour of the coarser grained samples is not very well constrained by our experiments with periods to 1020 s [2], the extrapolated behaviour at relatively long periods (>100 s) at high temperatures (>1300 °C) for large grain sizes (>10 mm) needs further experimental investigation.

Similarly, our experiments effectively place only an upper bound on the lower cutoff time, necessitating the introduction of the adjustment $\delta \ln J_U(d, T)$ (Eq. (7)). More detailed experiments at relatively low temperature (700–900 °C) are needed to document the attenuation associated with the cumulative dispersion at periods <1 s at higher temperatures.

We have already pointed out the need for a revision of the widely used Raj-Ashby model of grain boundary sliding [18,19] to resolve differences between the model predictions and experimental observations [21].

Finally the viscoelastic relaxation associated with stress-induced migration of dislocations (both dry and in the presence of water) needs to be investigated experimentally.

5.3. Grain size

Our experimental data clearly show the intrinsic grain size dependence of shear modulus and attenuation; therefore grain size needs to be specified in our model calculations. Common estimates of upper mantle grain sizes are in the mm to cm range (e.g. [55] and references therein); this is the grain size range used here. The grain size increase with depth is not uniquely constrained with the current modeling. For a constant grain size of 1 mm it would be difficult to find a mechanism to systematically increase the shear velocity below 200 km (Fig. 4e), but for a grain size of 5 cm the presence of water or melt could reduce velocity and Q in the LVZ. However, the water loss predicted by current models of mantle flow and melt generation at mid-ocean ridges would not readily explain the age dependent deepening and lessening of the LVZ up to ~80–100 My (e.g. [14]) shown by seismological models (Fig. 5).

A possible explanation for the increase in grain size with depth is a change in deformation mechanism. Karato and Wu [56] suggested that a transition from dislocation to diffusion creep occurs with increasing depth at about 200 km, depending on a range of conditions. Hirth and Kohlstedt [55] calculate a similar transition depth for a constant grain size of 1 cm; the transition depth is again dependent on a range of parameters in the flow laws. They point out that the grain size at a depth of 100 km would have to be <10 μm for diffusion creep to dominate. In the dislocation creep regime the grain size is determined by dynamic recrystallisation, whereas in the diffusion creep regime the grain size is largely determined by grain growth. Seismic anisotropy, which is produced only by dislocation creep, is observed to depths of about 160–200 km beneath the Pacific. It is therefore plausible that grain sizes in the shallow upper mantle, particularly at the relatively low temperatures in the plastically deforming portions of the thermal boundary layer, are smaller due to dynamic recrystallisation during dislocation creep. Grain sizes may be larger in the deeper upper mantle deforming predominantly by diffusion creep (but with a dislocation creep component, see discussion e.g. in [55]). For

continents with their thicker cold, high velocity lid and shallower temperature gradients in the lithosphere the transition may be more gradual and extend to greater depth as indicated by the greater depth of anisotropy [52] (Table 3).

5.4. Water

The effect of structurally bound water on the viscoelastic behavior of olivine has not yet been investigated experimentally; its possible significant influence is to some extent inferred by analogy with its effect on viscous behavior observed in finite-strain deformation experiments [57].

Karato and Jung [14] attribute the seismologically modeled sharpness of the velocity drop at 60–80 km below ocean basins (sometimes referred to as Gutenberg discontinuity) to the effect of water. However, in contrast to seismological models Karato and Jung's [14] dry thermal modelling, as well as that of Shapiro and Ritzwoller [53] and ours (Fig. 4) predicts a significant negative velocity gradient in the high velocity lid above the Gutenberg discontinuity, as this is the depth interval with the largest temperature gradients in the upper mantle. Gaherty et al. [36] describe the Gutenberg discontinuity as an impedance drop occurring within a depth interval of less than 30 km, with surface wave attenuation data consistent with but not requiring a large drop (p. 22305). A negative velocity gradient in the lid (decreasing the required velocity drop below) together with the enhanced velocity decrease at the onset of anelasticity at ~900 °C (see also Karato and Jung's [14] dry modelling) appears therefore consistent with a seismologically inferred impedance drop over a 30 km depth interval. A ubiquitous contribution of water to a drop in velocity below ocean basins is therefore not required; however, water may plausibly affect the velocity and attenuation structure for example at subduction zones.

5.5. Major element compositional variations

The primary origin of relatively large scale compositional variations in the upper mantle (e.g. the contrast between oceanic and cratonic continental lithosphere) is assumed to be partial melting and removal of the melt from "fertile" source rocks. Melt removal depletes the source rock of lower melting point components. Regarding shear modulus and density the important consequences are the simultaneous depletion of the residuum in FeO and Al_2O_3. To first order, FeO depletion increases the shear modulus of olivine (and orthopyroxene) and hence the shear velocity of the bulk rock, but decreases olivine and bulk rock density. The removal of Al_2O_3 decreases the proportion of the aluminous phase (garnet) in the whole rock. Since garnet is more dense and has a higher shear modulus than olivine and pyroxenes, a decrease in the garnet proportion decreases both the whole rock density and shear modulus.

The combined effects of simultaneous removal of FeO and Al_2O_3 on the shear modulus therefore tend to cancel each other (the olivine shear modulus increases while the garnet proportion decreases), while both garnet removal and decreasing iron content decrease the density. This was pointed out by Jordan [58] and has recently been substantially updated by Schutt and Lesher [59]. Jordan [58] and Schutt and Lesher [59] parameterize bulk rock compositional changes from experimental melting studies and find that there is essentially no change in shear velocity in the garnet stability field as a function of depletion with up to 40% melt removed (a change in olivine mode from 56% to 86%, Mg# ~90–93).

In a different approach, Lee [60] calculates seismic velocities and density of mantle rocks from the composition of natural peridotites with a range of compositions. The compositions of a significant number of the natural peridotites fall off the 'melting trend' defined by a correlated increase in Mg# and the proportion of olivine. The main cause in the scatter of the compositions is likely the re-fertilization by unrelated, secondary melts after primary melt extraction. Natural peridotites also originate from a range of pressure and temperature conditions. Assessing whether the compositional variability of individual xenoliths reflects localised or regional variations (at least on the length scale of surface waves of order of 100 km) is difficult. On a continental scale, a velocity increase of ~1.2% [60] associated with the extremes in the range in bulk Mg# (89–93) can not explain the velocity variation of >10% at 100–200 km depth between cratonic Western Australia and South Eastern Australia (Figs. 6 and 7).

A common result of both approaches is that the difference between olivine shear velocity and bulk

shear velocity is small (≤1%, [60], Table 1; [59], Tables 9 and 11) and not greatly affected by changes in bulk composition (anelasticity is not considered in these studies). The error associated with calculations based only on olivine shear velocity is therefore probably smaller than the uncertainties in most seismological models and the uncertainties in other parameters in the calculations.

An increasing proportion of garnet between 200 and 400 km could contribute to the shear velocity increase shown by seismological models in this depth range. However, Irifune and Ringwood [61] and Irifune [62] demonstrate that the progressive dissolution of pyroxene in garnet with increasing pressure for pyrolite bulk composition occurs mainly at pressures corresponding to depths of 400–480 km. The expected velocity increase for the depth range 200–400 km can be no greater than about 0.06 km/s.

Attenuation is likely to be even less sensitive to composition than shear velocity. Because Q is calculated from the ratio of the real and imaginary parts of the creep function, it is not a function of the unrelaxed compliance (J_U), i.e. does not depend on the (anharmonic) value of the shear modulus of the rock. Our experiments so far suggest that the grain boundary viscosity (the key parameter for attenuation due to grain boundary sliding [2,21]) does not vary significantly between high-purity sol–gel derived polycrystals and those saturated with olivine-incompatible trace elements. In more detail, grain boundaries in samples originating from San Carlos olivine contain detectable Ca, Al and Ti, while in grain boundaries of olivine of Sol–Gel origin no trace elements are detectable. Despite this compositional difference, we can not resolve any difference in attenuation or shear modulus (the major element composition of the olivine ($\sim Fo_{90}$) is the same for both types of sample). Therefore Q should be even less sensitive to composition than V_s and a primary indicator for lateral temperature variations in the absence of melt.

In summary, while shear velocity and Q are primarily dependent on temperature and grain size, combined seismological and gravity studies may better resolve lateral compositional variations in the upper mantle (e.g. [64,65]). The secondary effect of compositional relative to temperature variations on seismic velocities has also been found in a number of other studies (e.g. [5,7]).

5.6. Depth extent of cratons

A key question regarding the structure of continents is the thickness of lithosphere in cratonic areas [10]. Potential problems for surface-wave models in resolving the depth extent of cratons are their diminishing resolution with depth and the limited availability of models with paths that fall entirely into relatively uniform tectonic provinces. Seismological studies show at most a modest and very deep low velocity zone beneath old cratons [66–69]. A comparison of these shear wave models with velocity profiles calculated from our experimental data shows that for conductive geotherms that join the adiabat at depths less than 200 km a pronounced low velocity zone is unavoidable (Fig. 7). For geotherms joining the adiabat below 250–350 km depth a mild velocity decrease occurs at those depths, as seen in a number of seismological models. For V_s to be near constant throughout the upper mantle, the geotherm needs to join the adiabat deeper than 350 km. Seismological models showing velocities at 300–400 km depth in archean cratonic areas that are significantly higher than those for non-cratonic continental areas or beneath ocean basins suggest that temperatures beneath cratons are subadiabatic to transition zone depths.

Acknowledgements

We thank S. Karato and F. Deschamps for constructive reviews. Support for Ian Jackson from the Geodynamics Research Center, Ehime University, Matsuyama, Japan during a visit in 2003 is gratefully acknowledged. We thank Stewart Fishwick for providing the seismological model for Australia and surrounding oceans.

References

[1] B.H. Tan, I. Jackson, J.D. Fitz Gerald, High-temperature viscoelasticity of fine-grained polycrystalline olivine, Phys. Chem. Miner. 28 (2001) 641–664.

[2] I. Jackson, J.D. Fitz Gerald, U.H. Faul, B.H. Tan, Grain-size sensitive seismic wave attenuation in polycrystalline olivine, J. Geophys. Res. 107 (B12 2360) (2002), doi:10.1029/2001JB001225.

[3] E.D. Humphreys, K.G. Dueker, Physical state of the western U.S. upper mantle, J. Geophys. Res. 99 (1994) 9635–9650.

[4] K.P. Furlong, W. Spakman, R. Wortel, Thermal structure of the continental lithosphere: constraints from seismic tomography, Tectonophysics 244 (1995) 107–117.
[5] S.V. Sobolev, H. Zeyen, G. Stoll, F. Werling, R. Altherr, K. Fuchs, Upper mantle temperatures from teleseismic tomography of French Massif Central including effects of composition, mineral reactions, anharmonicity, anelasticity and partial melt, Earth Planet. Sci. Lett. 139 (1996) 147–163.
[6] S. Goes, R. Govers, P. Vacher, Shallow mantle temperatures under Europe from P and S wave tomography, J. Geophys. Res. 105 (B5) (2000) 11153–11169.
[7] F. Cammarano, S. Goes, P. Vacher, D. Giardini, Inferring upper-mantle temperatures from seismic velocities, Phys. Earth Planet. Inter. 138 (2003) 197–222.
[8] D.L. Anderson, J.B. Minster, The frequency dependence of Q in the earth and implications for mantle rheology and Chandler wobble, Geophys. J. R. Astron. Soc. 58 (1979) 431–440.
[9] S.-I. Karato, Importance of anelasticity in the interpretation of seismic tomography, Geophys. Res. Lett. 20 (15) (1993) 1623–1626.
[10] T.H. Jordan, The continental tectosphere, Rev. Geophys. 13 (1975) 1–12.
[11] M.A. Richards, W.-S. Yang, J.R. Baumgardner, H.-P. Bunge, Role of low viscosity zone in stabilizing plate tectonics: implications for comparative terrestrial planetology, Geochem. Geophys. Geosyst. 2 (2001), doi:10.1029/2000GC000115.
[12] A. Gutenberg, On the layer of relatively low wave velocity at a depth of about 80 kilometers, Bull. Seismol. Soc. Am. 58 (1948) 121–148.
[13] D.L. Anderson, C.G. Sammis, Partial melting in the upper mantle, Phys. Earth Planet. Inter. 3 (1970) 41–50.
[14] S.-I. Karato, H. Jung, Water, partial melting and the origin of the seismic low velocity and high attenuation zone in the upper mantle, Earth Planet. Sci. Lett. 157 (1998) 193–207.
[15] C. Goetze, A brief summary of our present day understanding of the effect of volatiles and partial melt on the mechanical properties of the upper mantle, in: M.H. Manghnani, S. Akimoto (Eds.), High Pressure Research: Applications in Geophysics, Center for Academic Publications, Tokyo, Japan, 1977, pp. 3–23.
[16] T.T. Gribb, R.F. Cooper, Low-frequency shear attenuation in polycrystalline olivine: grain boundary diffusion and the physical signficance of the Andrade model for viscoelastic rheology, J. Geophys. Res. 103 (B11) (1998) 27267–27279.
[17] B.H. Tan, I. Jackson, J.D. Fitz Gerald, Shear wave dispersion and attenuation in finegrained synthetic olivine aggregates: preliminary results, Geophys. Res. Lett. 24 (9) (1997) 1055–1058.
[18] R. Raj, M.F. Ashby, On grain boundary sliding and diffusional creep, Metall. Trans. 2 (1971) 1113–1127.
[19] R. Raj, Transient behaviour of diffusion induced creep and creep rupture, Metall. Trans., A, Phys. Metall. Mater. Sci. 6 (1975) 1499–1509.
[20] R.F. Cooper, Seismic wave attenuation: energy dissipation in viscoelastic crystalline solids, in: S. Karato, H. Wenk (Eds.), Plastic Deformation in Minerals and Rocks, Rev. Mineral. Geochem., vol. 51, Mineralogical Society of America, Washington, DC, 2003, pp. 253–290.
[21] U.H. Faul, J.D. Fitz Gerald, I. Jackson, Shear-wave attenuation and dispersion in melt-bearing olivine polycrystals: II. Microstructural interpretation and seismological implications, J. Geophys. Res. 109 (2004), doi:10.1029/2003JB002407.
[22] I. Jackson, U.H. Faul, J.D. Fitz Gerald, B.H. Tan, Shear-wave attenuation and dispersion in melt-bearing olivine polycrystals: I. Specimen fabrication and mechanical testing, J. Geophys. Res. 109 (2004), doi:10.1029/2003JB002406.
[23] A.S. Nowick, B.S. Berry, Anelastic Relaxation in Crystalline Solids, 1972, 677 pp.
[24] G. Ranalli, Rheology of the Earth, Chapman and Hall, London, UK, 1995, 413 pp.
[25] D.G. Isaak, High-temperature elasticity of iron-bearing olivines, J. Geophys. Res. 97 (B2) (1992) 1871–1885.
[26] O.L. Anderson, D.G. Isaak, Elastic constants of mantle minerals at high temperature, in: T.J. Ahrens (Ed.), Mineral Physics and Crystallography, A Handbook of Physical Constants, American Geophysical Union, Washington, USA, 1995, pp. 64–97.
[27] J.D. Bass, Elasticity of minerals, glasses and melts, in: T.J. Ahrens (Ed.), Mineral Physics and Crystallography, A Handbook of Physical Constants, American Geophysical Union, Washington, USA, 1995, pp. 45–63.
[28] D.W. Forsyth, Geophysical constraints on mantle flow and melt generation beneath mid-ocean ridges, Mantle Flow and Melt Generation at Mid-Ocean Ridges, Geophysical Monograph, vol. 71, American Geophysical Union, Washington, USA, 1999, pp. 1–65.
[29] D.L. Turcotte, G. Schubert, Geodynamics: Applications of Continuum Physics to Geological Problems, Wiley, New York, 1982, 450 pp.
[30] P. Gillet, P. Richet, F. Guyot, G. Fiquet, High-temperature thermodynamic properties of forsterite, J. Geophys. Res. 96 (1991) 11805–11816.
[31] H. Schmeling, G. Marquart, T. Ruedas, Pressure- and temperature-dependent thermal expansivity and the effect on mantle convection and surface observables, Geophys. J. Int. 154 (2003) 224–229.
[32] H. Fujisawa, N. Fujii, H. Mizutani, H. Kanamori, S.-I. Akimoto, Thermal diffusivity of Mg_2SiO_4, Fe_2SiO_4, and NaCl at high pressures and temperatures, J. Geophys. Res. 73 (14) (1968) 4727–4733.
[33] R.P. Denlinger, A revised estimate for the temperature structure of the oceanic lithosphere, J. Geophys. Res. 97 (B5) (1992) 7219–7222.
[34] D.S. Chapman, Thermal gradients in the continental crust, in: J.B. Dawson, D.A. Carswell, J. Hall, K.H. Wedepohl (Eds.), The Nature of the Lower Continental Crust, Geological Society Special Publication, vol. 24, 1986, pp. 63–70.
[35] C. Jaupart, J.C. Mareschal, The thermal structure and thickness of continental roots, Lithos 48 (1999) 93–114.
[36] J.B. Gaherty, T.H. Jordan, L.S. Gee, Seismic structure of the upper mantle in a central Pacific corridor, J. Geophys. Res. 101 (B10) (1996) 22291–22309.

[37] C.E. Nishimura, D.W. Forsyth, The anisotropic structure of the upper mantle in the Pacific, Geophys. J. 96 (1989) 203–229.
[38] S. Fishwick, B.L.N. Kennett, A. Reading, Contrasts in lithospheric structure within the Australian craton—insights from surface wave tomography, Earth Planet. Sci. Lett. 231 (2005) 163–176.
[39] A.M. Dziewonski, D.L. Anderson, Preliminary reference Earth model, Phys. Earth Planet. Inter. 25 (1981) 297–357.
[40] B. Romanowicz, A global tomographic model of shear attenuation in the upper mantle, J. Geophys. Res. 100 (1995) 12375.
[41] N.D. Selby, J.H. Woodhouse, The Q structure of the upper mantle: constraints from Rayleigh wave amplitudes, J. Geophys. Res. 107 (B5) (2002), doi:10.1029/2001JB000257.
[42] S.-I. Karato, D.C. Rubie, Toward an experimental study of deep mantle rheology: a new multianvil sample assembly for deformation studies under high pressures and temperatures, J. Geophys. Res. 102 (1997) 20111–20122.
[43] M.R. Drury, J.D. Fitz Gerald, Mantle rheology: insights from laboratory studies of deformation and phase transitions, in: I. Jackson (Ed.), The Earth's Mantle, Composition, Structure and Evolution, Cambridge University Press, Cambridge, 1998, pp. 503–560.
[44] C.G. Sammis, J.C. Smith, G. Shubert, A critical assessment of estimation methods for activation volume, J. Geophys. Res. 86 (1981) 10707–10718.
[45] Y.-S. Zhang, T. Lay, Evolution of oceanic upper mantle structure, Phys. Earth Planet. Inter. 114 (1999) 71–80.
[46] E. Debayle, B.L.N. Kennett, The Australian continental upper mantle: structure and deformation inferred from surface waves, J. Geophys. Res. 105 (B11) (2000) 25423–25450.
[47] J.H. Sass, A.H. Lachenbruch, Thermal regime of the Australian continental crust, in: M.W. McElhinny (Ed.), The Earth—Its Origin, Structure and Evolution, Academic Press, London, 1979, pp. 301–351.
[48] S. McLaren, M. Sandiford, M. Hand, N. Neumann, L. Wyborn, I. Bastrakova, Chapter 12—the hot southern continent: heat flow and heat production in Australian Proterozoic terranes, Spec. Publ.-Geol. Soc. Aust. 22 (2002) 151–161.
[49] G. Clitheroe, O. Gudmundsson, B.L.N. Kennett, The crustal thickness of Australia, J. Geophys. Res. 105 (B6) (2000) 13697–13713.
[50] R.L. Rudnick, W.F. McDonough, R.J. O'Connell, Thermal structure, thickness and composition of continental lithosphere, Chem. Geol. 145 (1998) 395–411.
[51] F.J. Simons, R.D. van der Hilst, Age-dependent seismic thickness and mechanical strength of the Australian lithosphere, Geophys. Res. Lett. 29 (2002) 1529–1533, doi:10.1029/2002GL014962.
[52] F.J. Simons, R.D. van der Hilst, J.-P. Montagner, A. Zielhuis, Multimode Rayleigh wave inversion for heterogeneity and azimuthal anisotropy of the Australian upper mantle, Geophys. J. Int. 151 (2002) 738–754.
[53] N.M. Shapiro, M.H. Ritzwoller, Thermodynamic constraints on seismic inversions, Geophys. J. Int. 157 (2004) 1175–1188.
[54] A. Shito, S.-I. Karato, J. Park, Frequency dependence of Q in Earths upper mantle inferred from continuous spectra of body waves, Geophys. Res. Lett. 31 (2004) L12603.
[55] G. Hirth, D. Kohlstedt, Rheology of the upper mantle and the mantle wedge: a view from experimentalists, Inside the Subduction Factory, Geophys. Monogr., vol. 138, 2003, pp. 83–105.
[56] S.-I. Karato, P. Wu, Rheology of the upper mantle: a synthesis, Science 260 (1993) 771–778.
[57] S.-I. Karato, M.S. Paterson, J.D. Fitz Gerald, Rheology of synthetic olivine aggregates: influence of grain size and water, J. Geophys. Res. 91 (1986) 8151–8176.
[58] T.H. Jordan, Mineralogies, Densities and Seismic Velocities of Garnet Lherzolites and their Geophysical Implications, American Geophysical Union, Washington, USA, 1979.
[59] D.L. Schutt, C.E. Lesher, The effects of melt depletion on the density and seismic velocity of garnet and spinel lherzolite, J. Geophys. Res. (submitted for publication).
[60] C.-T.A. Lee, Compositional variation of density and seismic velocities in natural peridotites at STP conditions: implications for seismic imaging of compositional heterogeneities in the upper mantle, J. Geophys. Res. 108 (B9) (2003), doi:10.1029/2003JB002413.
[61] T. Irifune, A.E. Ringwood, Phase transformations in primitive MORB and pyrolite compositions to 25 GPa and geophysical implications, in: M.H. Manghnani, Y. Sono (Eds.), In High Pressure Research in Geophysics, Terra Scientific, Tokyo, 1987, pp. 231–242.
[62] T. Irifune, Phase transformations in the Earth's mantle and subducting slabs; implications for their composition, seismic velocity and density structures and dynamics, Isl. Arc 2 (1993) 55–71.
[63] C. Gaina, R.D. Mueller, S.C. Cande, Absolute plate motion, mantle flow, and volcanism at the boundary between the Pacific and Indian Ocean Mantle Domains Since 90 Ma, The History and Dynamics of Global Plate Motions, Geophysical Monograph, vol. 121, American Geophysical Union, 2000, pp. 189–210.
[64] A.M. Forte, A.M. Dziewonsky, R.J. O'Connel, Thermal and chemical heterogeneity in the mantle: a seismic and geodynamic study of continental roots, Phys. Earth Planet. Inter. 92 (1995) 42–55.
[65] F. Deschamps, R. Snieder, J. Trampert, The relative density to shear velocity scaling in the uppermost mantle, Phys. Earth Planet. Inter. 124 (2001) 193–211.
[66] M. Freybourger, J.B. Gaherty, T.H. Jordan, K.S. Group, Structure of the Kaapvaal craton from surface waves, Geophys. Res. Lett. 28 (2001) 2489–2492.
[67] S.P. Grand, D.V. Helmberger, Upper mantle shear structure of North America, Geophys. J. R. Astron. Soc. 76 (1984) 399–438.
[68] Y. Kaiho, B.L.N. Kennett, Three-dimensional seismic structure beneath the Australasian region from refracted wave observations, Geophys. J. Int. 142 (2000) 651–668.
[69] N.M. Shapiro, M.H. Ritzwoller, Monte-Carlo inversion for a global shear—velocity model of the crust and upper mantle, Geophys. J. Int. 151 (2002) 88–105.